J Mater Sci: Mater Electron **(2024) 35:1023**

Novel injectable calcium-magnesium phosphate cement-based composites with piezoelectric properties: advancements in bone regeneration applications

Neslihan Sakar[1,*], Aylin Ziylan Albayrak[2], Merve Karakaya[3], Umut Adem[3], and Tunay Tansel[4]

[1] *Department of Nanoscience and Nanoengineering, Dokuz Eylul University, Izmir, Turkey*
[2] *Department of Metallurgical and Materials Engineering, Dokuz Eylul University, Izmir, Turkey*
[3] *Department of Materials Science and Engineering, İzmir Institute of Technology, Izmir, Turkey*
[4] *Institute of Nuclear Sciences/Photonics Division, Hacettepe University, Ankara, Turkey*

Received: 27 January 2024
Accepted: 13 May 2024
Published online: 28 May 2024

ABSTRACT

Designing a novel injectable bone cement is an important approach to the success of bone healing in minimally invasive surgeries. As natural bone has a piezoelectric property, which is crucial in bone regeneration, this study focused on the development of a novel injectable composite bone cement with piezoelectric properties. For the composite composition, calcium and zirconium doped barium titanate (BCZT) was used for its piezoelectric property, while calcium phosphate and magnesium phosphate cement (CMPC) were preferred for its bone-like properties. In this framework, first BCZT, CMPC, and their composites were prepared, and their phase structures, particle size distributions, and piezoelectric and dielectric properties were investigated. Then, the composite bone cements were prepared by mixing CMPC with BCZT in three different ratios (20%, 30%, and 40%). Next, polysorbate 80 solution was added to the cement mixtures to prepare the injectable pastes. Finally, injectability, setting time, and compressive strength of the composites were assessed. As a result, the composite bone cement containing 30% BCZT has the potential to be used as an injectable bone cement in invasive orthopedic surgery.

1 Introduction

Owing to the aging population, tissue trauma, and congenital diseases, bone fractures are gradually becoming a common medical problem. Bone tissue has a natural ability to heal itself in order to maintain its lifelong function. Bone healing depends on the age, genetic, environmental, and socioeconomic factors of a patient. In cases where bone healing is impaired, tissue scaffolds can support bone tissue regeneration in the damaged area and biodegrade after healing. Many studies have focused on designing bone scaffolds using

Address correspondence to E-mail: birinci.neslihan@gmail.com

https://doi.org/10.1007/s10854-024-12761-8

various biomaterials and/or methods for repairing damaged bone as tissue engineering strategies [1–6]. The desired property of a bone scaffold is that it can mimic the function and structure of a natural bone, which is composed of collagen fibers reinforced with bone minerals, predominantly hydroxyapatite (HA). Furthermore, this natural composite has a piezoelectric property [7]. The piezoelectric coefficient, d_{33}, of human bone was measured as 0.7 pC/N [8]. The piezoelectric property of bone leads to the development of surface charges when exposed to stress. This charge generation stimulates bone-building osteoblast cells regulating the cell cycle, migration, proliferation, and differentiation. Therefore, it can be stated that the use of piezoelectric biomaterials in bone tissue engineering enhances bone regeneration potential, and helps accelerate bone healing by mimicking natural bone [5, 6, 9–12]. Among the piezoelectric materials, barium titanate ($BaTiO_3$, BT) is widely utilized as a piezoelectric biomaterial [13–15], and its piezoelectric coefficient can be improved through ion doping, such as Sr^{2+}, Ca^{2+}, and Zr^{4+}. In this context, Ca^{2+} and Zr^{4+} doped BT (BCZT) is found to be one of the most prominent piezoelectric biomaterials with non-toxicity and biocompatibility [11, 16, 17]. In the study of Tang et al., HA/BT piezoelectric composites were prepared for bone regeneration. They found that the piezoelectric effect of BT promoted the growth of osteoblasts in vitro [18]. Also, Manohar et al. showed that HA-BCZT composites of different ratios demonstrated better bone cell growth than pristine HA samples and attributed the increase in bone cell proliferation to piezoelectricity [17].

On the other hand, bone cements are a great tool for mimicking natural bone owing to their similar mineral structure. They are particularly useful for treating complex bone damage. They can be injected directly into the damaged area through invasive surgery without the need for open surgery. They can easily adapt to bone damage locations and harden in vivo at the site where they are injected. In addition to these benefits, bone cements display unique properties like biocompatibility and biodegradability [1–3, 19]. Among them, calcium phosphate cement (CPC) and magnesium phosphate cement (MPC) stand as pivotal components for bone repair and regeneration. Meanwhile, injectable bone cement with a piezoelectric property has attracted increasing attention in recent years [20, 21] Tang et al. introduced BT and graphene into MPC to prepare a piezoelectric injectable bone cement. According to their in vitro studies, BT and graphene additions promoted biomineralization on the composite surface [20]. Koju et al. studied injectable bone cement composites, including BT and CPC. They stated that the addition of BT supported good injectability and biocompatibility [21].

In this study, our goal is to innovate by designing a novel injectable composite bone cement consisting of BCZT-added CPC-MPC (CMPC) with piezoelectric properties. This marks the first instance of combining CPC, MPC, and BCZT to create an injectable bone cement for treating bone defects. As the flow of the study, first CPC, MPC, and BCZT powders were produced. Then, their phase structures, particle size distributions, dielectric constants, and piezoelectric coefficients were analyzed by X-ray diffraction (XRD), particle size analyzer, LCR meter, and d_{33} meter, respectively. Finally, the injectability and setting time of the piezoelectric composite cements as well as their resulting compressive strengths were evaluated for their potential applications in orthopedic surgery.

2 Experimental method

The scheme representing the flow of the study is given in Fig. 1.

2.1 BCZT synthesis

The $xBa(Zr_{0.2}Ti_{0.8})O_3$-$(1-x)(Ba_{0.7}Ca_{0.3})TiO_3$ ($x = 0.5$) piezoelectric ceramic powder was synthesized using a sol–gel process with analytical reagent (AR) grade chemicals from Sigma Aldrich, including barium acetate ($Ba(CH_3COO)_2$), zirconium oxychloride ($ZrOCl_2.8H_2O$), calcium nitrate tetrahydrate ($Ca(NO_3)_2.4H_2O$), and titanium isopropoxide ($C_{12}H_{28}O_4Ti$). The amount of precursors was combined in stoichiometric ratios. Acetic acid was used as a solvent for barium acetate, and ethanol for zirconium oxychloride and calcium nitrate tetrahydrate. Each solution was prepared individually and then mixed. Next, the required amount of titanium isopropoxide was added to the mixture. The resulting precursor solution underwent continuous stirring and heating at 100 °C for approximately 4 h to form a gel precipitate. The obtained gel was first dried in an oven for 12 h and then calcined at 1000 °C for 4 h in ambient air to produce crystalline powders, following the procedures given in the literature [22, 23].

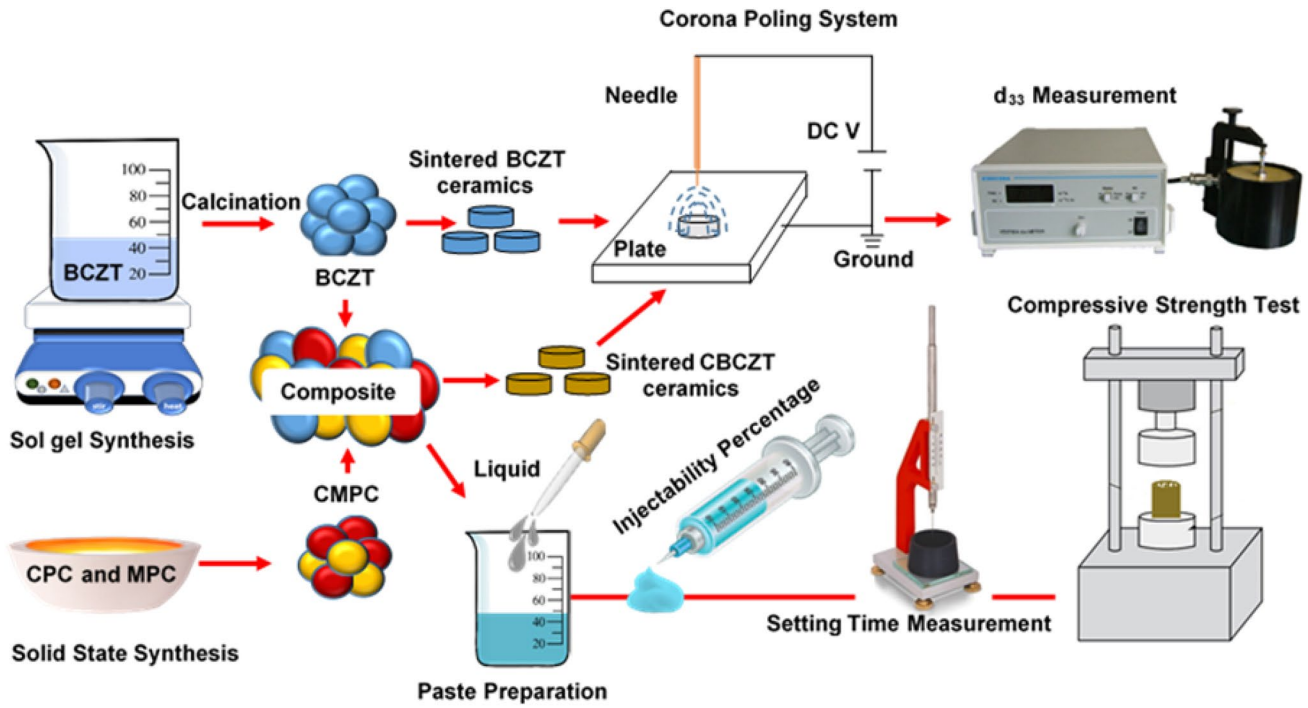

Fig. 1 Injectable bone cement preparation and characterization scheme

2.2 Preparation of CMPC

The primary components of CMPC powders were CPC and MPC with equal weight ratios. CPC is composed of tetra calcium phosphate ($Ca_4P_2O_9$, TTCP) and calcium phosphate anhydrous ($CaHPO_4$, DCPA) in an equal molar ratio. To produce TTCP, diammonium phosphate ($(NH_4)_2HPO_4$, Sigma Aldrich) and calcium carbonate ($CaCO_3$, Sigma Aldrich) were used as the raw materials, mixed in a 1:2 molar ratio. After the mixture was crushed in an agate mortar for a while, it was transferred to an alumina crucible and heat-treated at 1500 °C. Subsequently, it was quenched after holding for 15 h. On the other hand, calcium phosphate dehydrates ($CaHPO_4.2H_2O$) underwent heat treatment at 350 °C for 4 h to obtain DCPA. To prepare MPC, dead-burned magnesium oxide and diammonium phosphate ($(NH_4)_2HPO_4$, Sigma Aldrich) were mixed in a 3.8:1 molar ratio. Dead-burned MgO was produced by heat-treated magnesium oxide (light, %96, Alfa Aesar) at 1450 °C for 4 h.

2.3 Fabrication of CMPC-BCZT composites

The composites were produced by mixing CMPC with BCZT powders in distinct weight percentages (0%—CMPC, 20%—CBCZT20, 30%—CBCZT30, 40%—CBCZT40, and 100%—BCZT). The CMPC and BCZT powders were ground in various proportions using an agate mortar. A binder, polyvinyl alcohol (PVA), was added to the powder mixtures at 2.0% by weight (w/w). To measure dielectric and piezoelectric coefficients, pellet samples were fabricated. The mixtures with the binder were pressed into pellets in a 10 mm die at 300 MPa. The binder was burned out at 600 °C for 60 min with a heating rate of 1 °C/min. After burn-out, the CMPC, CBCZT20, CBCZT30, and CBCZT40 pellets were sintered at 1100 °C for 90 min, while the BCZT pellets were sintered at 1450 °C for 180 min at a heating rate of 2 °C/min. Archimedes' method was used for measuring the density of the sintered samples. Subsequently, the sintered pellets were polarized using the previously optimized parameters by a homemade corona system at an electric field of 7.5 kV/cm for 150 min at room temperature (RT) to induce their piezoelectric responses. Corona poling was also applied to both the silver paste-electroded and non-electroded samples.

2.4 Characterizations

Phase analysis of the powder and pellet samples was carried out using a Rigaku D/Max (2200/RC Model) X-ray diffractometer (XRD) with Cu – Kα radiation (1.5406 Å) of 2 °C/min in the range of 20°—80°. The peak data obtained from the XRD were evaluated using the X'Pert Highscore Plus program. Also, Gsas software was used for the refinement of BCZT. The particle size distribution was examined by using a Horiba LA-950 particle size analyzer. The dielectric constant and loss variation with frequency were determined using an E4980AL LCR meter (Keysight Technologies, Santa Clara, CA, USA) at RT, using the sample holder (aixACCT, TFA 423-7). The measurement was controlled with a LabVIEW program. TF analyzer (aixACCT TF Analyzer 1000, Aachen, Germany), in conjunction with high-voltage amplifier (TREK 610E, TREK, Medina, NY, USA) and laser-interferometer (SIOS Meßtechnik GmbH, Germany), was employed to generate polarization and strain loops under the alternating electric field which was in the form of a triangular wave with 10 Hz frequency. To determine the piezoelectric coefficient (d_{33}), samples were corona poled and then analyzed using a d_{33} meter (Sinocera Piezoelectronics, YE2730A, China) in which the applied force has an amplitude of 0.25 N with 110 Hz frequency. After crystal structure and electrical characterizations, the composite cements were evaluated for their injectability, setting time, and compressive strength using the following studies.

2.5 Paste preparations

The powder-to-liquid ratio (P/L), which can be defined as the use of liquid quantity for a specific mass of powder, is an important parameter that is effective on injectability, setting time, and the compressive strength of the samples. The injectable pastes were prepared by mixing CBCZT20, CBCZT30, CBCZT40, and CMPC (control sample) powders with a liquid solution according to the previously optimized P/L ratio of 1.55 g/ml. The liquid solution was prepared by mixing 3.0 wt% polysorbate 80 (Tween 80, Sigma Aldrich) and deionized water.

2.6 Injectability test

The powder and liquid were mixed for 3 min with a spatula and then transferred to a 2.5-ml disposable syringe with an internal nozzle diameter of 5.0 mm for an injectability test. The paste was manually injected until no paste was removed from the syringe. The percentage of injectability was determined by dividing the weight of the paste extruded through the syringe by the original weight of the paste in the syringe using Eq. 1. The average value was determined by performing each test three times.

$$\mathrm{INJ} = \frac{W_{\mathrm{injected}}}{W_{\mathrm{total}}} \times 100 \quad (1)$$

2.7 Setting time

The setting time was measured using a Vicat apparatus, according to ASTM Test Method C 187-98. The Vicat apparatus has a frame holding a rod (300 g) with a stainless-steel needle, 1 mm in diameter, attached to it. The cement samples were removed at 1.0 min intervals from the 100% relative humidity environment and positioned under the 1 mm needle point. The initial setting time (t_i) was recorded when the needle was 1 mm above the bottom, whereas the final setting time (t_f) was identified when the needle penetrated less than 1 mm into the cement. Each experiment was repeated three times and the average values were calculated.

2.8 Compressive strength

The pastes BCZT20, BCZT30, BCZT40, and CMPC (prepared with the P/L ratio used for injectability and setting time) were transferred to a stainless-steel mold using a spatula and molded in the dimensions of Ø10 × 15 mm^3. The molded samples were then immersed in Ringer's solution (0.9 wt. % NaCl), similar to the saline composition of human body fluid, at a temperature of 37 °C and hardened for 24 h. Hardened samples were removed from the solution and dried overnight at room temperature. To observe the time-dependent changes in mechanical behavior, we subjected both CMPC and CBCZT30 to the same procedure for 72 and 168 h. The compressive strength of the specimens was assessed using a universal testing

machine (AG-2000A, Shimadzu Autograph, Shimadzu Co. Ltd, Japan) at a loading rate of 1 mm per minute. Each group of samples was replicated three times, and the results were evaluated as means ± standard deviation (means ± STD).

3 Results and discussion

3.1 XRD phase analysis

The XRD patterns of the BCTZ powder and ceramic are shown in Fig. 2 a. Tetragonal and orthorhombic phases are not clearly seen, probably, due to the coexistence of the phases in the XRD pattern of BCZT. However, Rietveld refinement confirms the coexistence of orthorhombic (Amm2, 01-081-2200), and tetragonal (P4mm, JCPDS: 01-075-2120) phases in BCZT powders and ceramics (Fig. 2 b). The peak splitting at around 45° which is indexed to the diffraction peaks of $(022)_O/(200)_O$ and $(200)_T/(002)_T$ is attributed to the orthorhombic and tetragonal phases, similar to those described in the literature [24–27]. Besides, at about 66°, the formation of triplet $(004)_O/(040)_O/(222)_O$ indicates the presence of the orthorhombic phase [28], and the peak splitting of $(202)_T/(220)_T$ confirms the tetragonal phase of BCZT [29] The splitting of the peaks at 45° and 66° is shown in the inset images of Fig. 2 a. The lattice parameters obtained by Gsas are given in Table 1, and the fitted refinement graph is displayed in Fig. 2 b.

Table 1 Rietveld refinement results of BCZT ceramics

R_{wp}, GOF, χ^2	15.49%, 1.91, 3.65	
Crystallographic system	Tetragonal	Orthorhombic
Space group	*P4mm*	*Amm2*
Weight fraction (%)	66.3	33.7
a (Å)	3.9942(6)	3.9972(8)
b (Å)	3.9942(6)	5.6720(2)
c (Å)	4.0082(2)	5.6765(8)
Unit cell volume (Å^3)	63.932	128.703
Tetragonality (*c*/*a*)	1.0035	
Density (g/cm^3)	5.791	6.648

It can be observed that there is only a trace of impurity (marks with, *, symbol) in the powders calcined at 1000 °C, and the impurity phase is attributed to the orthorhombic $CaTiO_3$ phase (JCPDS:01-082-0229)[30]. However, after the BCZT pellet samples were sintered at 1450 °C, the impurity phase vanished completely, and a pure perovskite BCZT phase occurred. This indicated that the impurity phase diffused into BCZT lattices, forming a solid solution by sintering at 1450 °C [31]. Furthermore, as can be seen in the inset of Fig. 2 a, the splitting of the peak at about 45°, which is related to the orthorhombic and tetragonal phases of BCZT, indicated that Ca^{2+} ions successfully occupied Ba-sites, and Zr^{4+} ions occupied Ti-sites [19, 20].

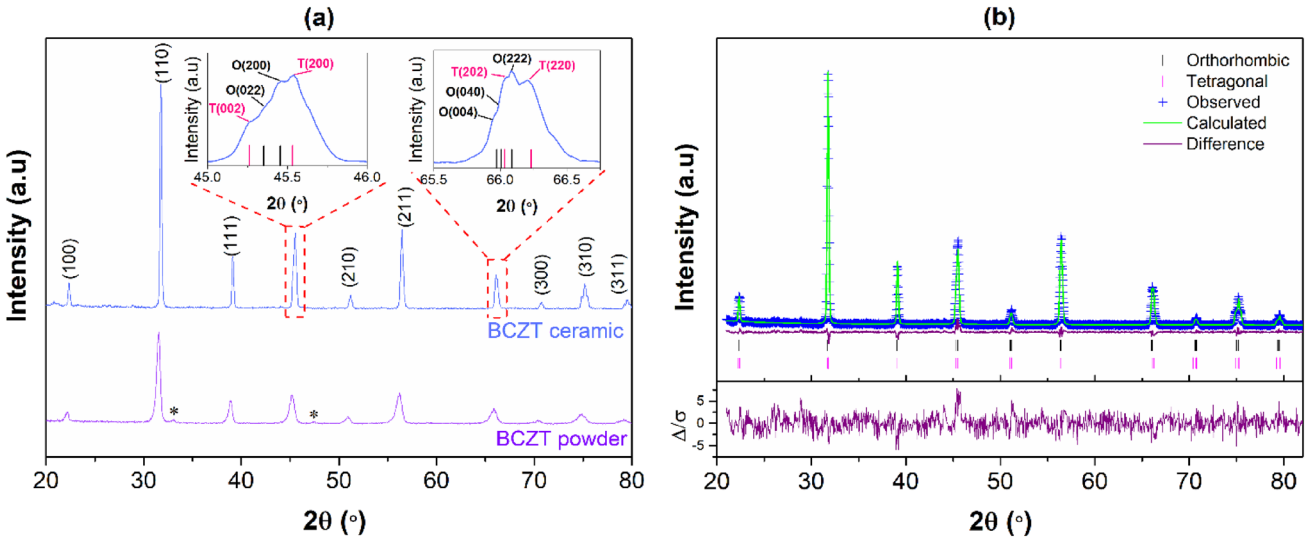

Fig. 2 **a** XRD patterns of the BCTZ powder and ceramic. The insets show the magnified area at 45° and 66°, **b** Fitted BCZT ceramic diffraction patterns obtained by Rietveld refinement

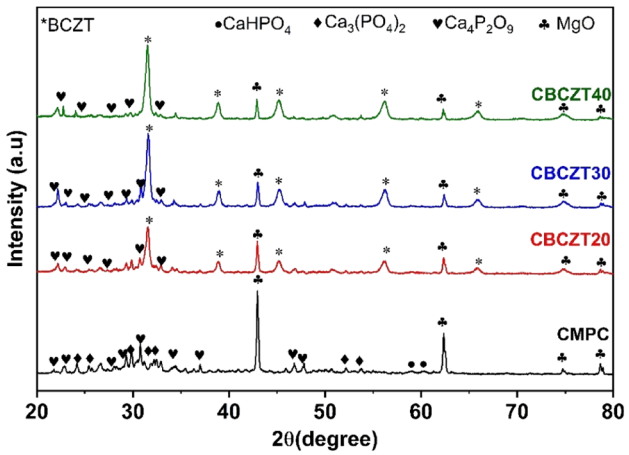

Fig. 3 XRD patterns of CMPC, CBCZT20, CBCZT30 and CBCZT40 composite powders showing multiple phases

The XRD patterns of the prepared composite powders are presented in Fig. 3. MgO (Periclase, JCPDS:00-045-0946), $Ca_4P_2O_9$ (TTCP, JCPDS:00-025-1137), Ca_3PO_4 (TCP, JCPDS:01-070-0364), and $CaHPO_4$ (JCPDS: 01-070-0360) are common phases in all the composites. The BCZT peaks are present in all the composites' XRD patterns except CMPC, as expected.

According to the XRD results in Fig. 4, the sintered pellet samples exhibit multiphase structures. For CMPC, the phases include periclase (MgO, JCPDS:00-045-0946), whitlockite ($Ca_{2.589}Mg_{0.411}O_8P_2$, JCPDS:01-087-582), stanfieldite ($Mg_3Ca_3(PO_4)_4$, JCPDS:01-073-1182), and hydroxyapatite (HA, $Ca_5HO_{13}P_3$, JCPDS:01-072-1243). Additionally, the XRD pattern of BCZT in CBCZT20, CBCZT30, and CBCZT40 composites is in good agreement with the JCPDS:01-079-2264. Figure 4 shows that the intensity of the major CMPC peak at ~43º decreased upon the addition of BCZT in the composites. Following the sintering process, CPC and MPC phases were combined to form the whitlockite and stanfieldite phases. However, no new phase formation was observed between BCZT and CMPC, suggesting that BCZT may play a piezoelectric role in the composites.

3.2 Particle size analysis

The particle size distribution curves for the BCZT, CPC, and MPC powders are illustrated in Fig. 5. While MPC displayed a narrower particle size distribution, CPC had a coarse-side shoulder. On the other hand, BCZT showed bimodal distribution which may be due to the agglomeration of the smaller particles.

Also, the span, median, and mean size values of the powders were measured. Span is a parameter that is used to measure the width of the particle size distribution. The span value and the width of particle size distribution have a direct correlation, suggesting that a decrease in the span value results in a narrower particle size distribution [32, 33]. BCZT, CPC, and MPC exhibited span values of 3.402, 2.800, and 2.163, respectively, meaning that particles in MPC have more similar sizes compared to those in BCZT and CPC. The median (d50) represents the middle value of the data set, indicating that half of the microparticles are

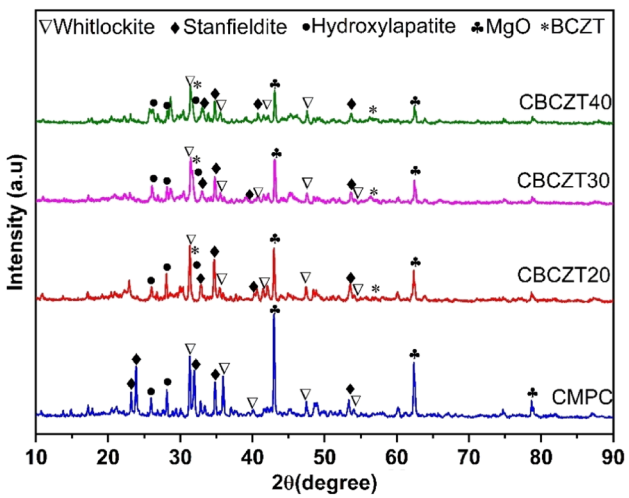

Fig. 4 XRD phase analysis results of the sintered composite ceramics

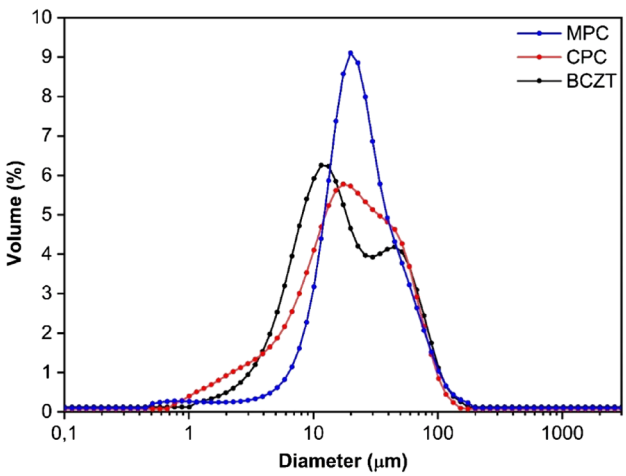

Fig. 5 Size distribution histograms of BCZT, CPC, and MPC powders

smaller than this value [34]. Median sizes for BCZT, CPC, and MPC were 15.060 μm, 17.820 μm, and 20.8622 μm, respectively. Besides, the mean values of BCZT, CPC, and MPC were 24.048 μm, 24.303 μm, and 27.190 μm, respectively.

3.3 Dielectric and piezoelectric behavior of the samples

The frequency-dependent dielectric constant properties of the samples at RT are presented in Fig. 6 a. The BCZT sample, in the morphotropic phase boundary region, exhibits a large dielectric constant and shows ferroelectric and piezoelectric properties evidenced by the ferroelectric hysteresis loop and corresponding and electric-field induced strain curve shown in Fig. 6 b. The d_{33} value (263 pC/N) of this sample confirms the high piezoelectric nature of the sample (see Table 2). CMPC shows low dielectric constant values in the range of 1–100 kHz, as expected [35]. Composite materials exhibit increased dielectric constant with the rise in BCZT compositional ratio, particularly evident at 100 kHz, where the dielectric constant reaches a plateau. (see Table 2). The dielectric loss values were recorded as 0.0217, 0.0016, 0.0061, 0.0207, and 0.0453 for BCZT, CMPC, CBCZT20, CBCZT30 and CBCZT40, respectively. The dielectric loss increases with increasing BCZT content as expected, in agreement with the increasing dielectric constant.

Prior to the d_{33} coefficient measurement, a poling process was applied to all samples to enhance their piezoelectricity by aligning the ferroelectric domains of a polycrystalline ceramic using a strong electric field [36]. The poling process is mainly performed in two ways: the contact (conventional) method and the corona method. In the contact method, both surfaces of the sample are electroded before polarization, for example using a silver paste, and the process is

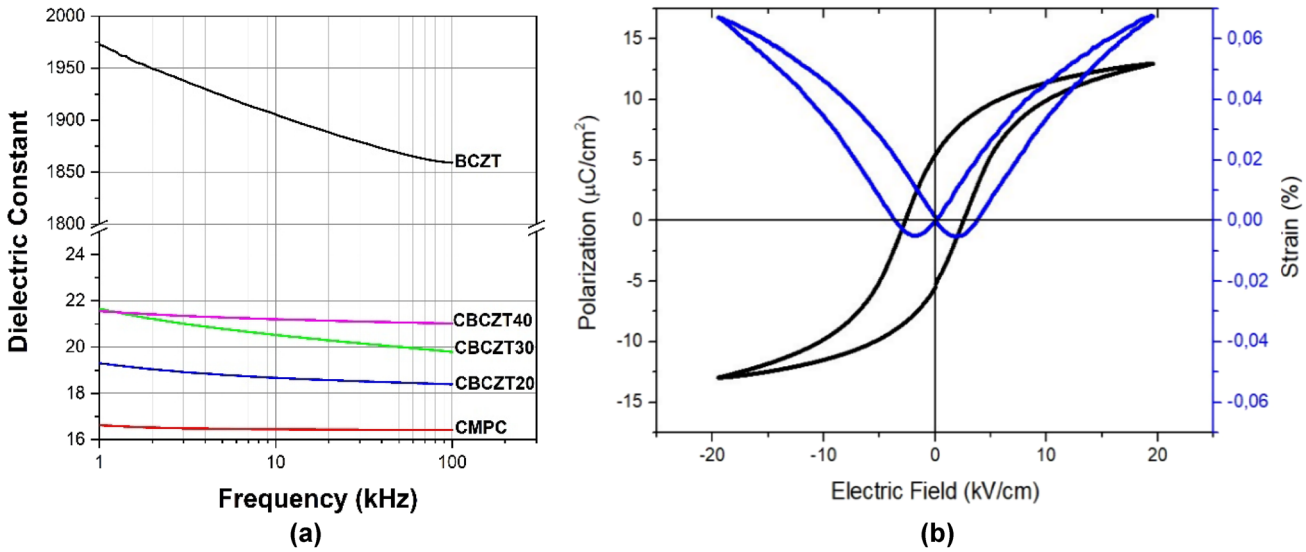

Fig. 6 **a** Presents the frequency-dependent dielectric constant of all samples at RT, and **b** shows the hysteresis loop and electric field-induced strain curve of BCZT

Table 2 Characterization results of the samples

Sample	d_{33} (pC/N)	ε_r	Injectability (%)	Setting time (minute)		Compressive Strength (MPa)		
				Initial	Final	24 h	72 h	168 h
CMPC	–	16.407	78,32	5	14	4.109 ± 0.54	4.284 ± 0.13	6.801 ± 0.51
CBCZT20	1.9	18.386	84,99	7	17	3.645 ± 0.47	–	–
CBCZT30	2.0	19.794	85,12	9	18	2.940 ± 0.65	3.484 ± 0.35	5.477 ± 0.39
CBCZT40	2.3	21.018	86,16	11	32	2.705 ± 0.37	–	–

carried out in a dielectric medium (usually silicone oil) to prevent the formation of sparks. In the corona method, on the other hand, the sample does not need to be electroded before polarization, and the polarization is performed in ionized air. Corona poling, which does not require electrodes and insulating liquids, is a non-contact and biologically safer electrical poling technique compared to typical contact piezoelectric ceramic polarization methods [37, 38]. Overall, non-contact poling offers several advantages over contact poling, particularly in terms of contamination prevention, damage reduction, uniformity improvement, and compatibility with sensitive materials [39].

A small increase in the dielectric constant up to 20 with increasing BCZT correlates with a slight increase in the piezoelectric coefficient of the composites (i.e. d_{33}). Precise measurements revealed an increase in the d_{33} coefficient ranging from 1.9 to 2.3 pC/N for composition ratios of 20–40% (Table 2). Importantly, the d_{33} coefficient of corona-poled samples remained unaffected by the presence or absence of a silver paste coating. Similarly, in the study conducted by Rotan et al. in 2020, it was indicated that silver coating the samples before polarization did not affect corona polarization. It was also emphasized that in the case of biomaterials, polarization without silver coating is important to avoid toxic effects [36].

BCZT is the piezoelectric constituent in the composites, with a piezoelectric coefficient of 263 pC/N. There is a similar study in literature that used a comparable content of piezoelectric additives achieving a d_{33} value of 2.53 pC/N for 40% piezoelectric additive [40]. On the other hand, the piezoelectric performance can be affected by the density of a ceramic. Samples with high density are expected to have higher piezoelectric performance due to the absence of lower permittivity pores [16]. The density values of 4.98, 1.94, 2.09, 2.42, and 2.60 g/mm^3 were measured for BCZT, CMPC, CBCZT20, CBCZT30, and CBCZT40, respectively. The variation of the d_{33} coefficient and the density of the samples with the BCZT content is shown in Fig. 7. As expected, both the density and d_{33} values increased with increasing the BCZT content.

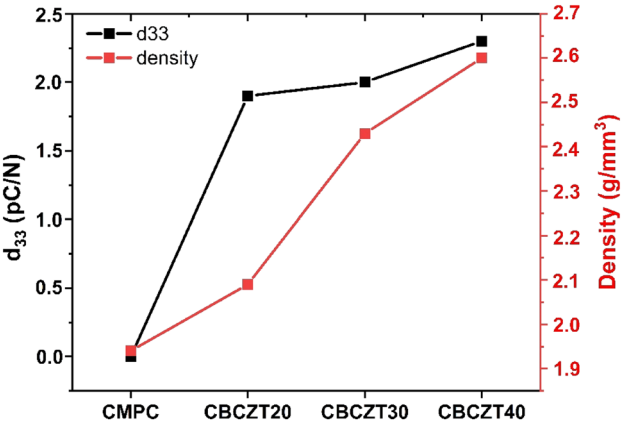

Fig. 7 Variation graph of the d_{33} coefficient and density as a function of BCZT content

3.4 Injectability and setting time

Injectability and setting time are crucial properties of a cement paste that affect its performance in invasive surgeries. These two properties are directly related to the setting kinetics of the cement paste. Phase transformation based on precipitation and dissolution activities leads to cement paste setting and hardening. When the hydrophilic cement particles are hydrated in water, a chemical reaction between cement and water begins. This hydration process, similar to that occurring in Portland cement, leads to hardening so that the cement has an enhanced mechanical strength over time. Moreover, the chemical composition of cement influences the chemical reactions during the setting process. In most cases, the addition of particles without setting capability affects the setting process of the injectable bone scaffold, resulting in delayed setting time but enhancing injectability [40]. In our study, the cement used in the composites was a 1:1 mixture of CPC and MPC, and the piezoelectric additive employed in the composites was BCZT. On the other hand, the P/L ratio has a significant effect on injectability and the setting times (***ti*** and ***tf***). The high liquid content in the paste increases the injectability but worsens the mechanical properties due to the formation of micro-pores. Conversely, reducing the water content below the optimum level causes packing irregularities and negatively affects the injectability and workability of bone cement during surgery [2, 41, 42]. As depicted in Fig. 8, the injectability increased with increasing BCZT addition as expected due to the inhibition of hydration reactions between the cement and water ions by the BCZT particles. Presumably, the presence of BCZT particles slows down the tendency for association between cement ions. Another reason for the good injectability of the prepared paste may be attributed to the particle size distribution. It can be said that the compatibility of the particle size

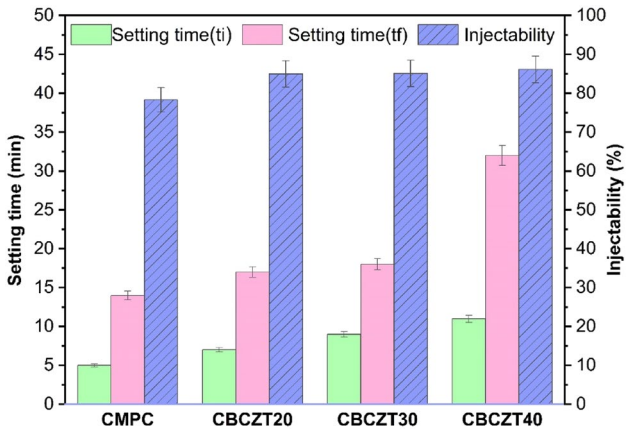

Fig. 8 Injectability and setting time (***ti*** and ***tf***) of the cements at a fixed P/L ratio of 1.55 g/ml

distribution of the components is of great importance for injectability. The results of the particle size distribution (see Fig. 5) show that the particles are in harmony with each other.

In orthopedic surgery, the time from preparation to injection of the paste into the damaged tissue is crucial and it is correlated with the initial setting time (***ti***) when the cement starts to lose its plasticity. The injection of the paste should be completed before ***ti***. On the other hand, at ***tf***, the cement hardens sufficiently and gains a certain structural strength. The wound should be closed after ***tf***. In the literature, the recommended ***ti*** is approximately 8 min and ***tf*** is approximately 15 min [43, 44] When ***ti*** and ***tf*** values of the samples were compared, CMPC had the lowest values with 4 min and 14 min, respectively. CBCZT20 and CBCZT30 showed similar ***ti*** and ***tf***, values, while CBCZT40 had ***ti*** of 11 min and ***tf*** of 32 min. Considering that the P/L ratio didn't change, the increase in BCZT in the composites delayed the hydration reactions of the cement. Therefore, an increasing BCZT ratio caused an increase in ***ti*** and ***tf*** values (see Fig. 8 and Table 2).

3.5 Compressive strength

Bone scaffolds are designed to support the healing of damaged bone tissue. Therefore, tissue scaffolds should resemble natural bone in many aspects such that they should also be compatible with the mechanical properties of the area in which they are used. The bones in the human body exhibit different mechanical properties depending on their structure and function. These mechanical properties are typically expressed in terms of compressive strength. The compressive strength values of the different bone types are as follows: human trabecular bone (30 MPa) [44], cortical bone (90 to 209 MPa), and cancellous bone (1.5 to 45 MPa) [45].

Compressive strength values for CMPC, CBCZT20, CBCZT30, and CBCZT40 after 24 h of hydration are presented in Fig. 9 a, and Table 2. CMPC demonstrated the highest compressive strength with a value of 4.109 ± 0.54 MPa. It is seen that the compressive

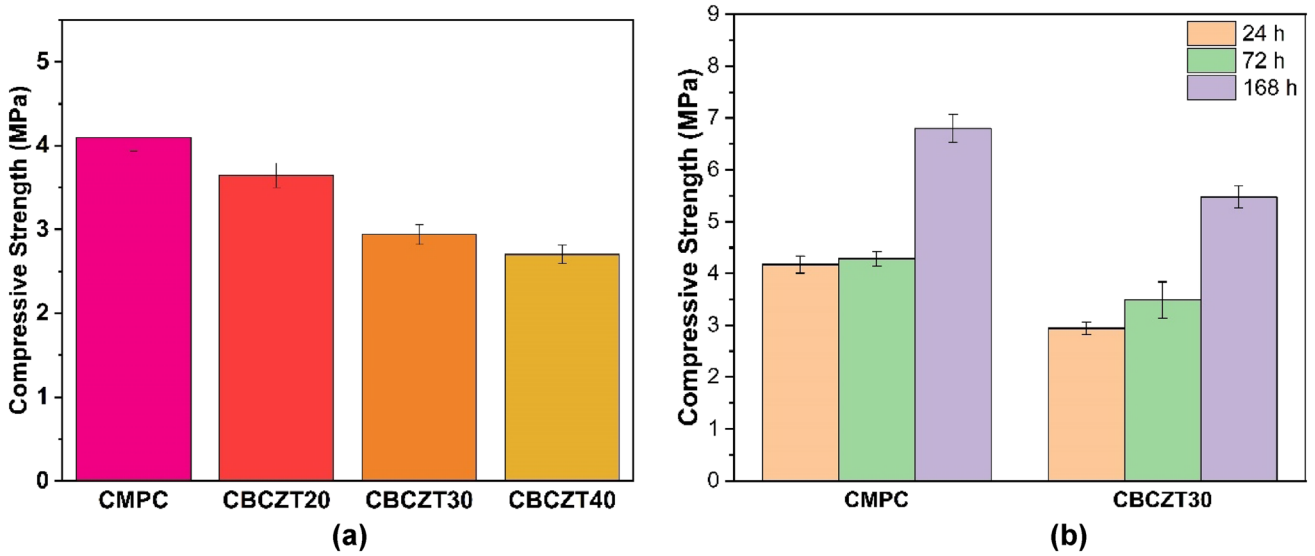

Fig. 9 **a** The compressive strength of the cements after 24 h, and **b** the compressive strength of CMPC and CBCZT30 after 24 h, 72 h, and 168 h

strength of the composite samples decreased with increasing BCZT content. One possible explanation for the decrement trend is that non-hydrating BCZT when used in small amounts in the composites may be surrounded by the hydrating CPC and MPC particles. However, hydration became more challenging with the increase in the BCZT ratio, and the compressive strength decreased while the setting time increased. Additionally, Fig. 9 b illustrates compressive strengths as a function of hydration time for CMPC and CBCZT30. CMPC was chosen as the control sample, while CBCZT30 was preferred for its good injectability, suitable setting times (*ti* and *tf*), and relatively higher d_{33} coefficient. According to the results, the compressive strength of both CMPC and CBCZT30 samples was enhanced with the increasing reaction time. However, it is seen that BCZT addition slowed down the increase in the compressive strength of CMPC. Nevertheless, the compressive strength values of both CMPC and CBCZT30 samples are within the 1.5–45 MPa range, which is suitable for cancellous bone. Besides, it is also worth noting that the BCZT addition improved the injectability of the CMPC cement as well as the regeneration potential of the damaged bone due to its piezoelectric property.

Phase transformation of CMPC cement with or without BCZT was evaluated after hydrating for 0 h, 24 h, 72 h, and 168 h by using XRD analysis (see Fig. 10). As can be seen in Fig. 10 a, the TTCP (JCPDS: 00-025-1137) and MgO (JCPDS: 00-045-0946) peaks are the most dominant in the anhydrate (0 h) CMPC sample. However, upon hydration for 24 h, HA (JCPDS: 01-072-1243) and struvite ($NH_4MgPO_4.6H_2O$, JCPDS: 00-015-0762) phases formed in small proportions in CMPC. As expected, the peak intensities of the HA and struvite phases gradually increased after 72 h and 168 h. A probable explanation for the phase change is that TTCP was converted to HA as a result of hydration, while MgO was converted to struvite [43, 46].

In the XRD pattern of CBCZT30 given in Fig. 10b, struvite, TTCP, HA, BT, and periclase (MgO) phases were identified. As the peaks of HA and BCZT are at 2θ 31.741° (HA, JCPDS: 01-072-1243) and 2θ 31.598° (BCZT, JCPDS: 01-081-2198), they probably overlapped under the highest peak at 2θ 31.651° in the XRD pattern. Considering that the BCZT ratio in the composite was constant, the slight increase in the intensity of the highest peak might be attributed to the gradual formation of the HA phase during the soaking time.

4 Conclusion

The primary objective of this study is to introduce a new injectable composite bone cement composition consisting of piezoelectric BCZT and CPC-MPC bone cement. This composition holds potential for applications in bone tissue engineering. BCZT, synthesized through the sol–gel method, exhibits a ferroelectric property, containing tetragonal and orthorhombic

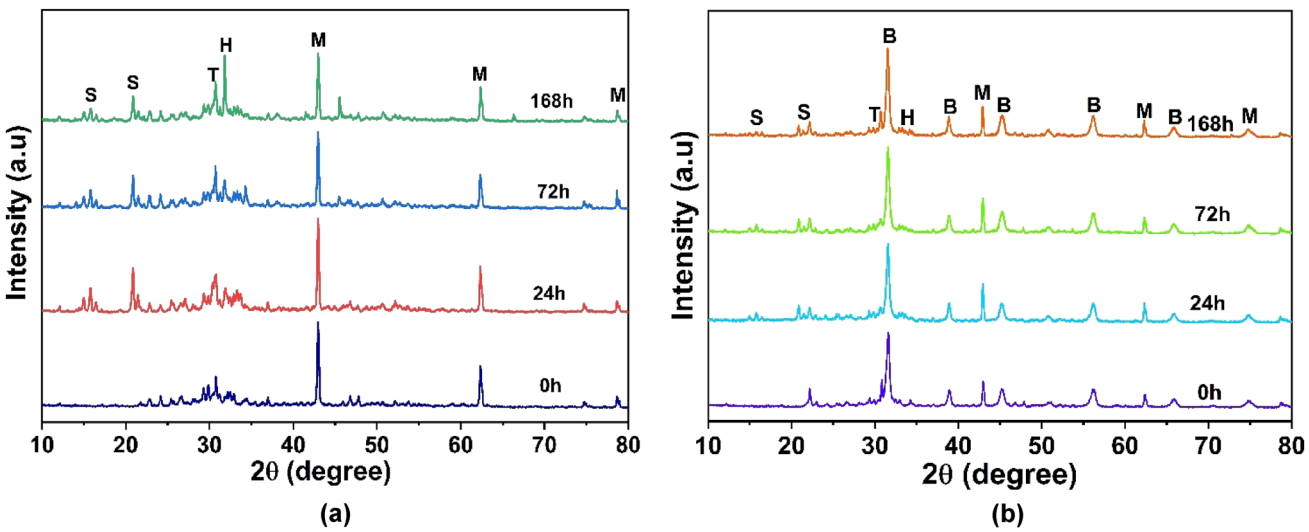

Fig. 10 **a** XRD pattern of CMPC and CBCZT30 and, **b** after soaking in water for 0–168 h

crystal structures. The d_{33} coefficient of BCZT was measured as 263 pC/N. Thus, the prepared composites with three different ratios of BCZT, namely CBCZT20, CBCZT30, and CBCZT40, showed piezoelectric properties with the d_{33} coefficients of 1.9 pC/N, 2.0 pC/N, and 2.3 pC/N, respectively.

All the composite cements prepared at a constant P/L ratio of 1.55 g/ml showed good injectability over 70%, which is required in invasive surgery, and this property was enhanced with increasing BCZT ratios. However, BCZT addition delayed the setting reaction, and therefore setting times were gradually increased. In addition, compressive strength values decreased upon increasing BCZT, but they were within the 1.5–45 MPa range which is sufficient for cancellous bone.

When the results of injectability, setting time, and mechanical strength of all the composite samples were considered, CBCZT30 was evaluated as the optimum injectable composite bone cement composition. It also exhibited a piezoelectric coefficient higher than that of natural bone which is 0.7 pC/N. Consequently, this novel bone cement composition is found to be promising in bone healing applications by invasive surgery.

Acknowledgements

This study is financially supported by TUBITAK—Short-Term R&D Funding Program (Project Number 222M340). The authors are indebted to the infrastructural support from Dokuz Eylul University, the Center for Production and Applications of Electronic Materials (EMUM) where the research was carried out. Also, Neslihan Sakar is supported by the Turkish Higher Education Council's 100/2000 Ph.D. Fellowship and TUBITAK 2211-C National PhD Scholarship Program.

Author contributions

Neslihan Sakar; Visualization, Investigation, Writing—Original draft preparation, Methodology, Resources. Aylin Ziylan Albayrak; Visualization, Investigation, Supervision, Writing- Reviewing and Editing, Methodology, Resources. Merve Gunnar; Writing—Original draft preparation, Methodology, Resources. Umut Adem; Supervision, Writing—Reviewing and Editing, Resources. Tunay Tansel; Visualization, Investigation, Supervision, Writing—Reviewing and Editing.

Funding

Open access funding provided by the Scientific and Technological Research Council of Türkiye (TÜBİTAK). Funding was supported by Türkiye Bilimsel ve Teknolojik Araştırma Kurumu, Grant Nos. (222M340, 2211-C).

Data availability

Authors confirm that all relevant data are included in the article and/or its supplementary information files.

Declarations

Conflict of interest The authors declare that they have no conflict of interest.

References

1. F. Chen, Z. Song, C. Liu, J. Mater. Chem. B **3**, 9173 (2015)
2. E. Şahin, D.M. Kalyon, J. Mech. Behav. Biomed. Mater. **72**, 252 (2017)
3. S.Y. Kim, S.H. Jeon, J. Ind. Eng. Chem. **18**, 128 (2012)
4. E.B. Montufar, Y. Maazouz, M.P. Ginebra, Acta Biomater. **9**, 6188 (2013)
5. M. Tavangar, F. Heidari, R. Hayati, F. Tabatabaei, D. Vashaee, L. Tayebi, Ceram. Int. **46**, 9086 (2020)

6. K. Kapat, Q.T.H. Shubhra, M. Zhou, S. Leeuwenburgh, Adv. Funct. Mater. (2020). https://doi.org/10.1002/adfm.201909045
7. E. Fukada, I. Yasuda, J. Phys. Soc. Japan **12**, 1158 (1957)
8. A.J. Bur, J. Biomech. **9**, 495 (1976)
9. S.-W. Yu, S.-T. Kuo, W.-H. Tuan, Y.-Y. Tsai, C.-H. Su, Mater. Lett. **65**, 3522 (2011)
10. D. Khare, B. Basu, A.K. Dubey, Biomaterials **258**, 120280 (2020)
11. T. Tariverdian, A. Behnamghader, P. Broukimilan, H. Barzegar-Bafrooei, M. Mozafari, Ceram. Int. **45**, 14029 (2019)
12. D. D'Alessandro, C. Ricci, M. Milazzo, G. Strangis, F. Forli, G. Buda, M. Petrini, S. Berrettini, M.J. Uddin, S. Danti, Biomolecules **11**, 1731 (2021)
13. Y. Zhang, L. Chen, J. Zeng, K. Zhou, D. Zhang, Mater. Sci. Eng. C **39**, 143 (2014)
14. X. Zhang, C. Zhang, Y. Lin, P. Hu, Y. Shen, K. Wang, S. Meng, Y. Chai, X. Dai, X. Liu, Y. Liu, X. Mo, C. Cao, S. Li, X. Deng, L. Chen, ACS Nano **10**, 7279 (2016)
15. F.J. Vouilloz, M.S. Castro, G.E. Vargas, A. Gorustovich, M.A. Fanovich, Ceram. Int. **43**, 4212 (2017)
16. K.K. Poon, M.C. Wurm, D.M. Evans, M.A. Einarsrud, R. Lutz, J. Glaum, J. Biomed. Mater. Res. - Part B Appl. Biomater. **108**, 1295 (2020)
17. C.S. Manohar, B.S. Kumar, S.P.P. Sadhu, S.K. Srimadh, V.S. Muthukumar, S. Venketesh, K.B.R. Varma, Nanotechnol. Rev. **8**, 61 (2019)
18. Y. Tang, C. Wu, Z. Wu, L. Hu, W. Zhang, K. Zhao, Sci. Rep. **7**, 1 (2017)
19. D. Wang, Y. Zhang, Z. Hong, Ceram. Int. **40**, 9799 (2014)
20. Y. Tang, C. Wu, P. Zhang, K. Zhao, Z. Wu, Ceram. Int. **46**, 12626 (2020)
21. N. Koju, P. Sikder, B. Gaihre, S.B. Bhaduri, Materials (Basel). **10**, 1258 (2018)
22. J.P. Praveen, T. Karthik, A.R. James, E. Chandrakala, S. Asthana, D. Das, J. Eur. Ceram. Soc. **35**, 1785 (2015)
23. E. Chandrakala, J. Paul Praveen, B. K. Hazra, and D. Das, Ceram. Int. **42**, 4964 (2016).
24. N.P.M.J. Raj, N.R. Alluri, G. Khandelwal, S.-J. Kim, J. Alloys Compd. **871**, 159503 (2021)
25. N.P.M.J. Raj, N.R. Alluri, G. Khandelwal, S.-J. Kim, Chem. Eng. J. **414**, 128840 (2021)
26. A. Patra, A. Pal, S. Sen, Ceram. Int. **44**, 11196 (2018)
27. X. Wang, Y. Huan, Y. Zhu, P. Zhang, W. Yang, P. Li, T. Wei, L. Li, X. Wang, J. Adv. Ceram. **11**, 184 (2022)
28. V. Bijalwan, I. Sokolov, P. Tofel, J. Asian Ceram. Soc. **9**, 229 (2021)
29. S. Yan, Z. Cao, Q. Liu, Y. Gao, H. Zhang, G. Li, J. Alloys Compd. **923**, 166398 (2022)
30. W. Li, Z. Xu, R. Chu, P. Fu, G. Zang, Curr. Appl. Phys. **12**, 748 (2012)
31. P. Wang, Y. Li, Y. Lu, J. Eur. Ceram. Soc. **31**, 2005 (2011)
32. C. Kirby-Smith, J. Steenekamp, D. Steyn, A. Haasbroek-Pheiffer, H. Hamman, J. Hamman, Appl. Sci. **13**, 4822 (2023)
33. R. Govoreanu, H. Saveyn, P. Van der Meeren, I. Nopens, P.A. Vanrolleghem, Water Sci. Technol. **60**, 1857 (2009)
34. G.C. Türkoğlu, G. Erkan, S.Y. Karavana, A.M. Sarıışık, A. Çetmeli Bakadur, B. Ütebay, A. Popescu, AATCC J. Res. **10**, 332 (2023)
35. O. Kaygili, S. Keser, T. Ates, S. Kirbag, F. Yakuphanoglu, Medziagotyra **22**, 65 (2016)
36. M. Rotan, M. Zhuk, J. Glaum, J. Eur. Ceram. Soc. **40**, 5402 (2020)
37. H. Xu, Y. Zhuang, Z. Fu, J. Cui, S. Jiang, B. Zhao, K. Lin, Ceram. Int. **50**, 672 (2024)
38. E.R. Cholleti, I.O.P. Conf, Ser. Mater. Sci. Eng. **455**, 012038 (2018)
39. T. Tansel, S. Ener Rusen, A. Rusen, Rev. Sci. Instrum. (2013). https://doi.org/10.1063/1.4773566
40. T. Wu, X. Ji, Z. Zhang, S. Wang, J. Zhou, L. Meng, X. Liu, H. Yu, T. Gong, Y. Liu, Ceram. Int. **49**, 19746 (2023)
41. M.P. Hofmann, A.R. Mohammed, Y. Perrie, U. Gbureck, J.E. Barralet, Acta Biomater. **5**, 43 (2009)
42. M. Bohner, G. Baroud, Biomaterials **26**, 1553 (2005)
43. F. Wu, J. Wei, H. Guo, F. Chen, H. Hong, C. Liu, Acta Biomater. **4**, 1873 (2008)
44. J. Jansen, E. Ooms, N. Verdonschot, J. Wolke, Orthop. Clin. North Am. **36**, 89 (2005)
45. M.P. Ginebra, Cements Bone Repair Mater. (2009). https://doi.org/10.1533/9781845696610.2.271
46. E.F. Burguera, H.H.K. Xu, M.D. Weir, J. Biomed. Mater. Res. - Part B Appl. Biomater. **77**, 126 (2006)